In Situ Formation of Heterojunction in Composite Lithium Anode Facilitates Fast and Uniform Interfacial Ion Transport

Shan Fang, Huasong Wang, Shangquan Zhao, Miaomiao Yu, Xiang Liu, Yong Li, Fanglin Wu, Wenhua Zuo, Naigen Zhou,* and Gregorio F. Ortiz**

Lithium metal is a highly promising anode for next-generation high-energy-density rechargeable batteries. Nevertheless, its practical application faces challenges due to the uncontrolled lithium dendrites growth and infinite volumetric expansion during repetitive cycling. Herein, a composite lithium anode is designed by mechanically rolling and pressing a cerium oxide-coated carbon textile with lithium foil (Li@CeO_2/CT). The in situ generated cerium dioxide (CeO_2) and cerium trioxide (Ce_2O_3) form a heterojunction with a reduced lithium-ion migration barrier, facilitating the rapid lithium ions migration. Additionally, both CeO_2 and Ce_2O_3 exhibit higher adsorbed energy with lithium, enabling faster and more distributed interfacial transport of lithium ions. Furthermore, the high specific surface area of 3D skeleton can effectively reduce local current density, and alleviate the lithium volumetric changes upon plating/stripping. Benefiting from this unique structure, the highly compact and uniform lithium deposition is constructed, allowing the Li@CeO_2/CT symmetric cells to maintain a stable cycling for over 500 cycles at an exceptional high current density of 100 mA cm^{-2}. When paired with $LiNi_{0.91}Co_{0.06}Mn_{0.03}O_2$ (NCM91) cathode, the cell achieves 74.3% capacity retention after 800 cycles at 1 C, and a remarkable capacity retention of 81.1% after 500 cycles even at a high rate of 4 C.

1. Introduction

The demand for high-energy rechargeable batteries has grown exponentially, particularly in the realm of portable electronic devices and electric vehicles.[1–3] Lithium metal stands out as a promising anode to improve the energy density of the secondary batteries in virtue of its high theoretical specific capacity (≈3860 mAh g^{-1}), the lowest electrochemical potential (−3.04 V vs. standard hydrogen electrode), and a low ionization energy (5.39 eV).[4–9] However, the uncontrolled lithium dendrite growth and the continuous volumetric changes during repeated Li plating/stripping pose challenges.[10,11] These issues lead to the cyclic collapse and regeneration of the solid-electrolyte interphase (SEI),[12,13] continually consumption of electrolyte and active Li, the formation of dead Li with an increase in cell resistance, ultimately resulting in low Coulombic efficiency and fast capacity decay.[14,15]

In order to address the above issues, researchers have put much efforts on revealing the failure mechanism of lithium metal batteries and proposing various strategies to overcome these challenges.[16–21] One common strategy is the liquid electrolyte engineering, i.e., the introduction of functional additives or modifications of electrolyte components to construct more robust SEI for reversible of lithium plating/stripping.[22,23] Another strategy is designing a stable artificial SEI (ASEI) on the surface of lithium metal to homogenize Li ion flux, and regulate the lithium deposition behavior, as well as building a high Young's modulus protective layer to inhibit the formation of lithium dendrites.[24–26] However, these two modification routes failed to achieve uniform lithium deposition at high current densities (>10 mA cm^{-2}). Particularly, at higher current densities, the migration rate of lithium ions cannot match rapid electron transfer, forming a concentration polarization near the electrode surface, where lithium ions

S. Fang, H. Wang, S. Zhao, M. Yu, X. Liu, Y. Li, N. Zhou
School of Physics and Materials Science
Nanchang University
Nanchang, Jiangxi 330031, China
E-mail: ngzhou@ncu.edu.cn

F. Wu
State Key Laboratory of Advanced Technology for Materials Synthesis and Processing
Wuhan University of Technology
Wuhan 430070, China
E-mail: fanglin-wu@whut.edu.cn

W. Zuo
Helmholtz Institute Ulm (HIU)
89081 Ulm, Germany

W. Zuo
Karlsruhe Institute of Technology
76021 Karlsruhe, Germany

G. F. Ortiz
Xiamen Key Laboratory of Optoelectronic Materials and Advanced Manufacturing, Institute of Luminescent Materials and Information Displays, College of Materials Science and Engineering
Huaqiao University
Xiamen 361021, China
E-mail: gregorio.ortiz@hqu.edu.cn

are depleted, intensifying the electric field strength, and resulting in the aggregation of lithium ions at the hotspot, leading to dendrite formation. 3D lithium metal hosts and surface modifications can reduce the effective local current density, decrease the electrochemical polarizations and accommodate volume variation during cycling, achieve uniform plating and stripping of lithium metal.[27,28]

Various 3D host designs utilize carbon materials, characterized by their low density, high electrical conductivity, substantial flexibility and mechanical strength, and easy to functionalize the surface.[29,30] Tu et al.[31] employed zinc oxide to modify carbon cloth, subsequently introducing molten lithium to create a novel composite anode with a straw-stack-like structure. The composite anode demonstrated lower voltage hysteresis and a stable SEI compared to bare lithium. Gao et al.[32] adorned carbon cloth (CC) with uniformly distributed Pb nanoparticles. Then, molten lithium was introduced into highly lithiophilic Pb@CC. The resulting composite anode achieved an exceptionally long cycle life of 4684 h in a symmetric cell. Nevertheless, the fabrication of structured lithium metal anode using the molten lithium adsorption method necessitates stringent preparation conditions. This process demands a controlled environment devoid of water and oxygen as well as at high-temperature (300 °C). Utilizing electrochemical methods to pre-deposit a specific capacity of lithium metal for constructing a structured composite lithium anode is also considered as an effective strategy. For instance, in our previously reported research, aluminum oxide was coated on the surface of hollow carbon fibers with pre-depositing 4 mAh cm^{-2} of lithium to constructed mismatch-conductivity composite anode. This 3D lithium anode, exhibited remarkable cycling stability in the full cell with low negative/positive ratio.[33] However, the electrochemical deposition approach inevitably produces a small amount of dead lithium because the stripping is not 100% efficient, and the larger comparative area of the 3D structure triggers side reactions that consume the electrolyte. Hence, the necessity for a preparation method that is both facile in operation and practicably applicable in industrial production is paramount. Furthermore, there is a need for further investigation into the plating/stripping mechanism of 3D structured electrodes in the vertical direction, particularly under high current density conditions. Understanding how to optimize the utilization of the specific surface area provided by the 3D skeleton is fundamental.

Here, we designed a highly efficient Li@CeO_2/CT composite anode employing a straightforward mechanical rolling and pressing method. The uniform CeO_2-modified carbon textile (CeO_2/CT) was created through a hydrothermal method. Following the electrochemical activation process of the Li@CeO_2/CT, an in situ heterojunction composed of cerium dioxide (CeO_2) and cerium trioxide (Ce_2O_3) was generated, both exhibit higher adsorbed energy with lithium (denoted as Li@CeO_x/CT), act as a guidance for uniform transport of lithium ions. Moreover, our observations indicate that the heterojunction effectively reduces the lithium-ion migration barrier, thereby facilitating rapid lithium-ion migration at the two-phase interface. This unique structural attribute enables uniform plating/stripping of lithium across the surface of the composite carbon fiber, fully exploiting with the 3D skeleton's specific surface area. Notably, this design prevents the formation of bulk or dendritic lithium in the void space. The electrochemical performance of the symmetrical cell is particularly noteworthy, showcasing the ability to cycle at an exceptionally high current density of 100 mA cm^{-2} for 500 cycles. When coupled with an NCM91 cathode, a significant 81.1% capacity retention is achieved after 500 cycles at 4 C. These remarkable results underscore the full potential of this composite anode for enhanced performance in energy storage applications.

2. Results and Discussion

2.1. Characterizations of Li@CeO_2/CT

To increase the hydrophilicity of carbon textile (CT), the CT surface was modified by enveloping a CeO_2 layer, which was achieved via a hydrothermal reaction following with heating treatment. Specifically, the CT was first immersed in mixed acid (H_2SO_4: HNO_3 = 1:1vol.%) to achieve complete dispersion in water and uniform distribution of CeO_2 on its surface. The scanning electron microscopy (SEM) images of raw and acid-treated CT and corresponding elemental mapping of nitrogen are shown in Figure S1 (Supporting Information), showing that the surface content of nitrogen on acid-treated CT obviously increases. The CeO_2/CT was then subjected to mechanical rolling, pressing, and cutting to finally form Li@CeO_2/CT composite anode disks for cell assembly, as displayed in **Figure 1a**. The XRD patterns of acid-treated CT and CeO_2/CT are compared in Figure 1b. The strong and sharp peaks that appear at 28.6°, 47.5°, and 56.3° are highly coincident with CeO_2 (PDF#97-062-1710), demonstrating the successful synthesis of CeO_2. Meanwhile, the significant reduction of peak intensity at 26° and 44° (which belong to the CT) in the CeO_2@CT sample hints a uniform loading of CeO_2 on the CT surface, thus weakened the CT peaks. The comparison of SEM images between CT and CeO_2/CT (Figure 1c,d) clearly exhibited the enriched CeO_2 on the CT surface, and the elemental mapping of O and Ce further certifies the uniform distribution of CeO_2 on the CT surface.

2.2. Electrochemical Behavior among Different Electrodes

To evaluate the effect of CT and CeO_2 on lithium deposition behavior of the Li@CeO_2/CT anode, the plating/stripping tests were conducted in symmetric cells using pure lithium, Li@CT and Li@CeO_2/CT as electrodes in carbonate-based electrolyte. A high cycling stability of symmetric Li@CeO_2/CT cell is exhibited at 2 mAh cm^{-2} (15 mA cm^{-2}) and 1 mAh cm^{-2} (2 mA cm^{-2}) in Figure S2 (Supporting Information), in contrast, the voltage of symmetric pure lithium cell starts to dramatically increase after ≈250 h, while the short circuit occurs after 400 h in symmetric Li@CT cell. To evaluate the high-rate capability of the composite anode, the cells were performed at exceptionally high current density of 20, 50, 100 mA cm^{-2} at 4 mAh cm^{-2}, as displayed in **Figure 2a–c**. At 20 mA cm^{-2} and 2 mAh cm^{-2}, the overpotential rapidly increases to around 1 V for symmetric pure lithium cell (green), and then gradually decreases, but remains in a fluctuating trend. After only 10 h, lithium dendrites pierced the separator resulting in the short circuit of cells. In comparison, the Li@CT (blue) can maintain cycling ≈250 h, accompanied by a gradual increase in polarizing voltage, and subsequently, a rapid short

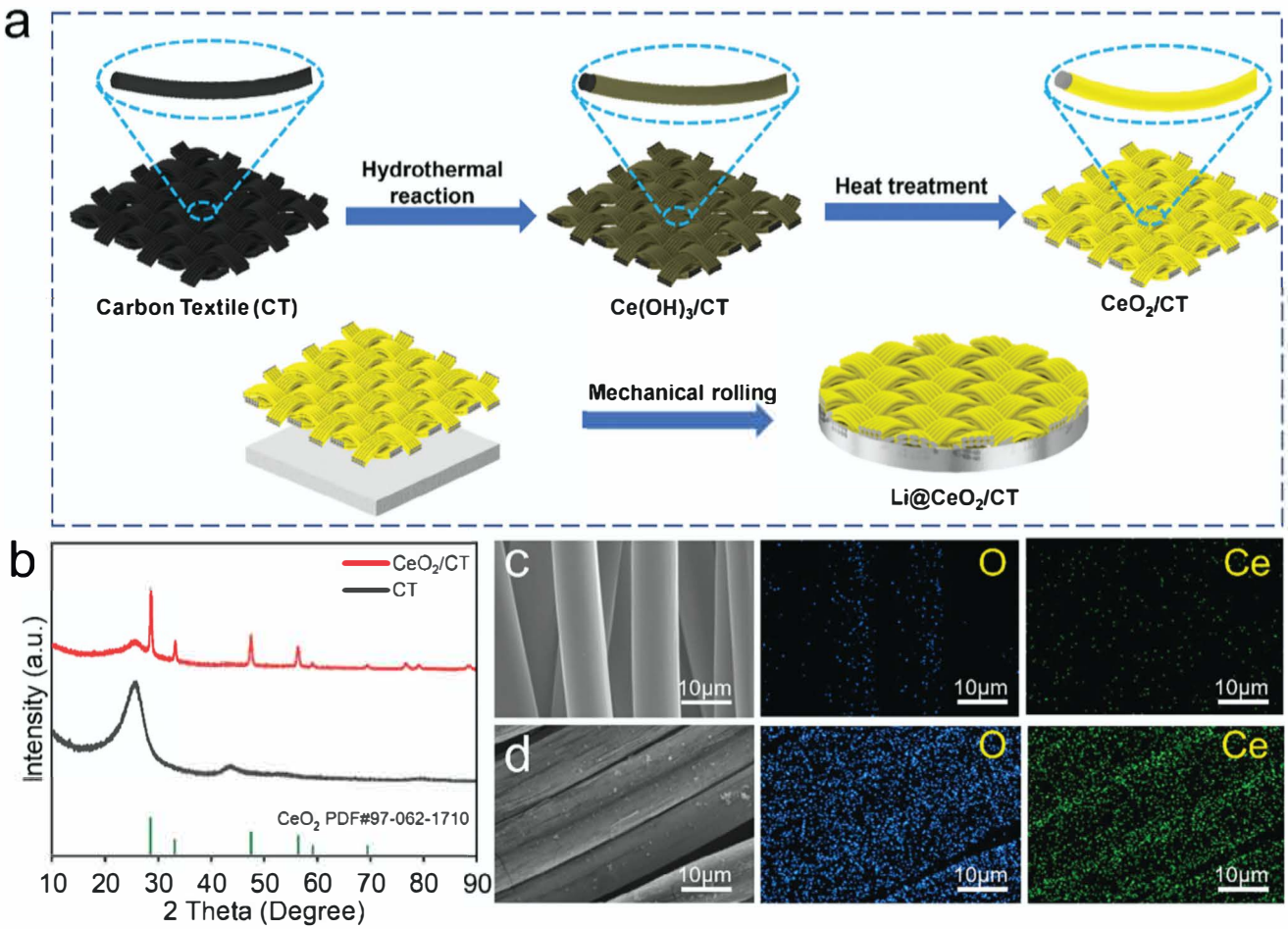

Figure 1. Preparation and characterization of Li@CeO_2/CT. a) Schematic illustration of the fabrication of Li@CeO_2/CT. b) XRD patterns of CT and CeO_2/CT. SEM images and corresponding O, Ce elemental mappings of c) acid treatment CT and d) CeO_2/CT.

circuit occurred. Differently, the Li@CeO_2/CT (red) cell exhibits stable cycling for >1500 cycles (300 h) without short circuit. This difference is even amplified at the higher current densities of 50 and 100 mA cm^{-2}, in which both symmetric pure lithium cells and Li@CT cells are unable to cycle. Surprisingly, the Li@CeO_2/CT cell still exhibits remarkable cycling stability and maintains a low overpotential of <0.5 V for >500 cycles even at ultra-high current density of 100 mA cm^{-2}, which demonstrates the fast kinetic behavior of Li ion transport for this special designed construction, probably attributed to the synergistic effect of the high specific surface area of the 3D cross-linked network and the uniform loading of CeO_2 on the fiber surface. Meanwhile, the CT||Li and CeO_2/CT||Li cells were assembled to determine the Coulombic efficiencies of the composite anodes (Figure 2d). The high and stable CE close to 100% was obtained in CeO_2/CT cell, reveals a highly reversible lithium deposition formed on the CeO_2/CT. In contrast, the CE of CT cells sharply fluctuated away from 100%. The exchange current densities (J^0) of three different anodes were performed by Tafel curves to evaluate the electrochemical kinetics at the electrode/electrolyte interface (Figure 2e). A clearly higher value of 1.07 mA cm^{-2} of CeO_2/CT was calculated compared to pure Li (0.51 mA cm^{-2}) and CT (0.83 mA cm^{-2}), which suggests a faster mass transfer and lower surface diffusion barrier at the CeO_2/CT electrode, contributing to a more efficient electrochemical reaction and lower overpotential. To further investigate the interface barrier for lithium ion transport, the activation energies of lithium diffusion in the SEI film (E_{SEI}) were determined by the fitting of EIS results the at different temperatures (Figure S3, Supporting Information), where the Li^+ activation energy on the SEI film follows the Arrhenius' law (Figure 2f). The activation energy of Li@CeO_2/CT and Li@CT (45.51 kJ mol^{-1}, 38.52 kJ mol^{-1}) is obviously lower than that of pure lithium (68.98 KJ mol^{-1}), this confirms the introduction of CT skeleton could clearly reduce interfacial energy barrier for lithium transport. The activation energy of Li@CeO_2/CT is slightly higher than that of Li@CT, possibly due to the lithiation reaction between CeO_2 and lithium in the initial stage, resulting in a higher activation energy for the initial lithium ions to traverse the SEI.

2.3. Deposition Morphology Analysis

To acquire a deeper understanding of the lithium deposition behavior on the composite anodes, the symmetric batteries with different electrodes were assembled and discharged at constant

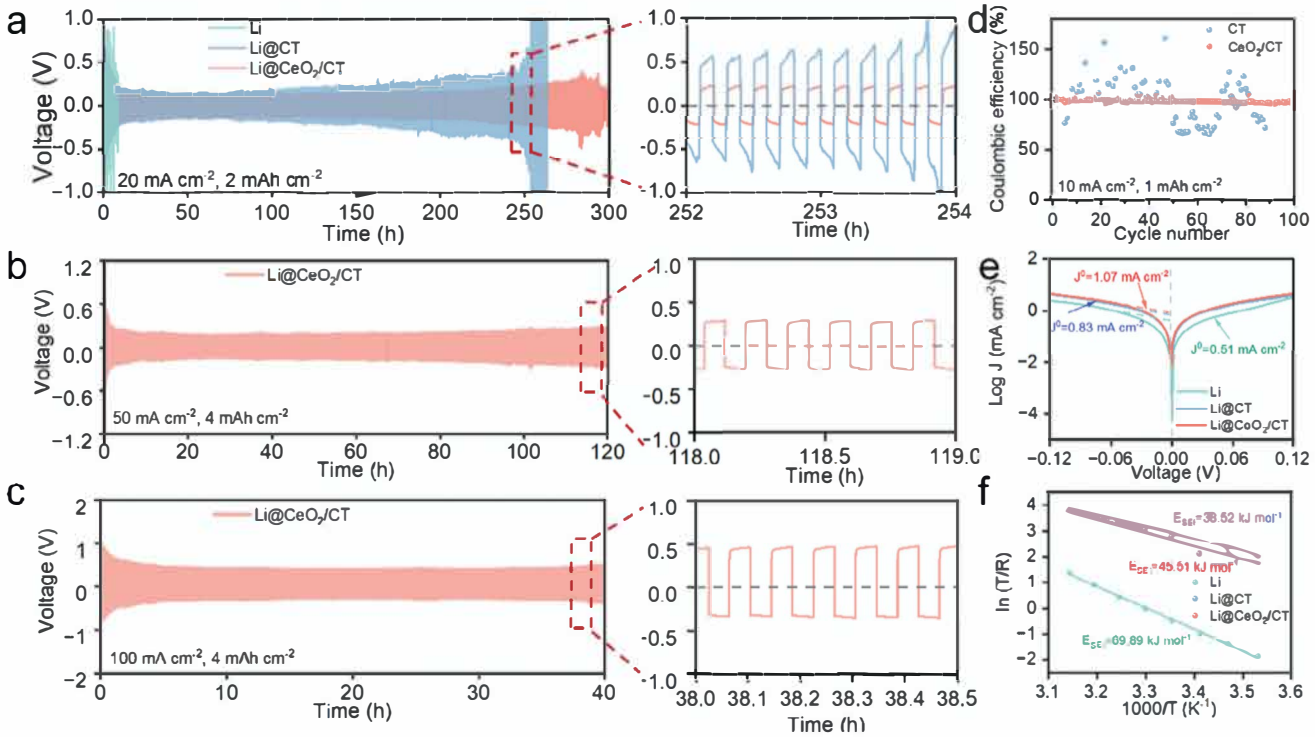

Figure 2. Plating/stripping behavior of symmetrical batteries with different electrodes at a) 20 mA cm^{-2},1 mAh cm^{-2}, b) 50 mA cm^{-2}, 4 mAh cm^{-2}, and c) 100 mA cm^{-2}, 4 mAh cm^{-2}. d) Coulombic efficiencies of CT and CeO_2@CT at 10 mA cm^{-2} for 100 cycles. e) Exchange current density obtained based on Tafel curve of different symmetric cells. f) Activation energy of SEI interface on different lithium metal anodes (calculated based on EIS data of symmetric cells tested at 10–45 °C, see Figure S3, Supporting Information).

current, meanwhile, the morphology of lithium deposition on the electrodes was in situ detected by using optical microscopy (5 mA cm^{-2}, **Figure 3**a–c). The figures exhibit that the surface of all the three electrodes appeared preliminary lithium deposition after initial 5 min of deposition. Specially, the pure lithium surface came out some irregular "moss-like" clumps that growing with the deposition time. Regarding the Li@CT, a gradually color evolution was observed from amaranth to silver, additionally, on the electrode surface of a partial covering which is probably associated with the lithium deposition and dead lithium. Differently, almost no difference can be detected in the Li@CeO_2/CT electrode, it is well confirmed the uniform lithium deposition along the CeO_2/CT fibers due to the contribution from cerium oxides.

The SEM characterization was also performed to determine the morphology of cycled electrodes after reduplicative plating/stripping. The symmetric cells were operated at a current density of 1 mA cm^{-2} and lithium deposition capacity of 1 mAh cm^{-2}. After one cycle, the surface of pure lithium (Figure 3d) exhibits irregular network-wire on the lithium metal surface with uneven lithium growth. For the Li@CT anode (Figure 3e), partial lithium accumulates on the fibers rather than deposited along the fibers, however, which is difficult to detect in Li@CeO_2/CT electrodes (Figure 3f), where the surfaces of Li@CeO_2/CT fibers are attached with dense and uniform lithium. When the cells were further plating/stripping to 20 cycles, the morphology difference among these cycled electrodes are magnified, as seen in the pure lithium electrode (Figure 3g), a thick coating layer mainly composed of lithium deposited products and dead lithium, accompanying with serious cracks which much increased the interface resistance. When shifting the focus to the Li@CT electrodes (Figure 3h), the lithium deposited products have heavily covered on the fibers disabling the lithium deposition along with fibers, this is accordant with the result from in situ optical microscopy. In comparison, the Li@CeO_2/CT electrode still maintains an unambiguous fiber shape without partial large-scale lithium coverage, suggesting the lithium uniformly deposited along the fibers. Figure S4 (Supporting Information) displays the SEM of the anode deposition morphology of symmetric cells at 50 and 100 mA cm^{-2} after cycling for 130 and 60 h, respectively. From the SEM, we can observe that even at such high current density, there is no dendrite formation on the surface of the composite electrode, further demonstrated the fast Li ion diffusion kinetic in the heterojunction of CeO_2/Ce_2O_3. In addition, half-cells were assembled to systematically assess the effect of CeO_2/CT on the nucleation behavior of lithium (Figure S5, Supporting Information). Pure lithium served as the counter electrode, while CeO_2/CT, CT, and pure copper foil were employed as the working electrodes for pairing and assembly. In order to establish a stable interface layer, the electrodes underwent an initial lithiation treatment (0.05-1.5 V charge/discharge for five cycles at 1 mA cm^{-2}). Notably, both CeO_2/CT and CT demonstrated relatively low lithium nucleation overpotentials, measuring 34 and 29 mV, respectively. The nucleation overpotential of CeO_2/CT is a little higher than CT, which is consist with the activation energy of Li ion diffusion in SEI. In contrast, the copper foil exhibited a significantly higher overpotential of 162 mV. This observed disparity in nucleation

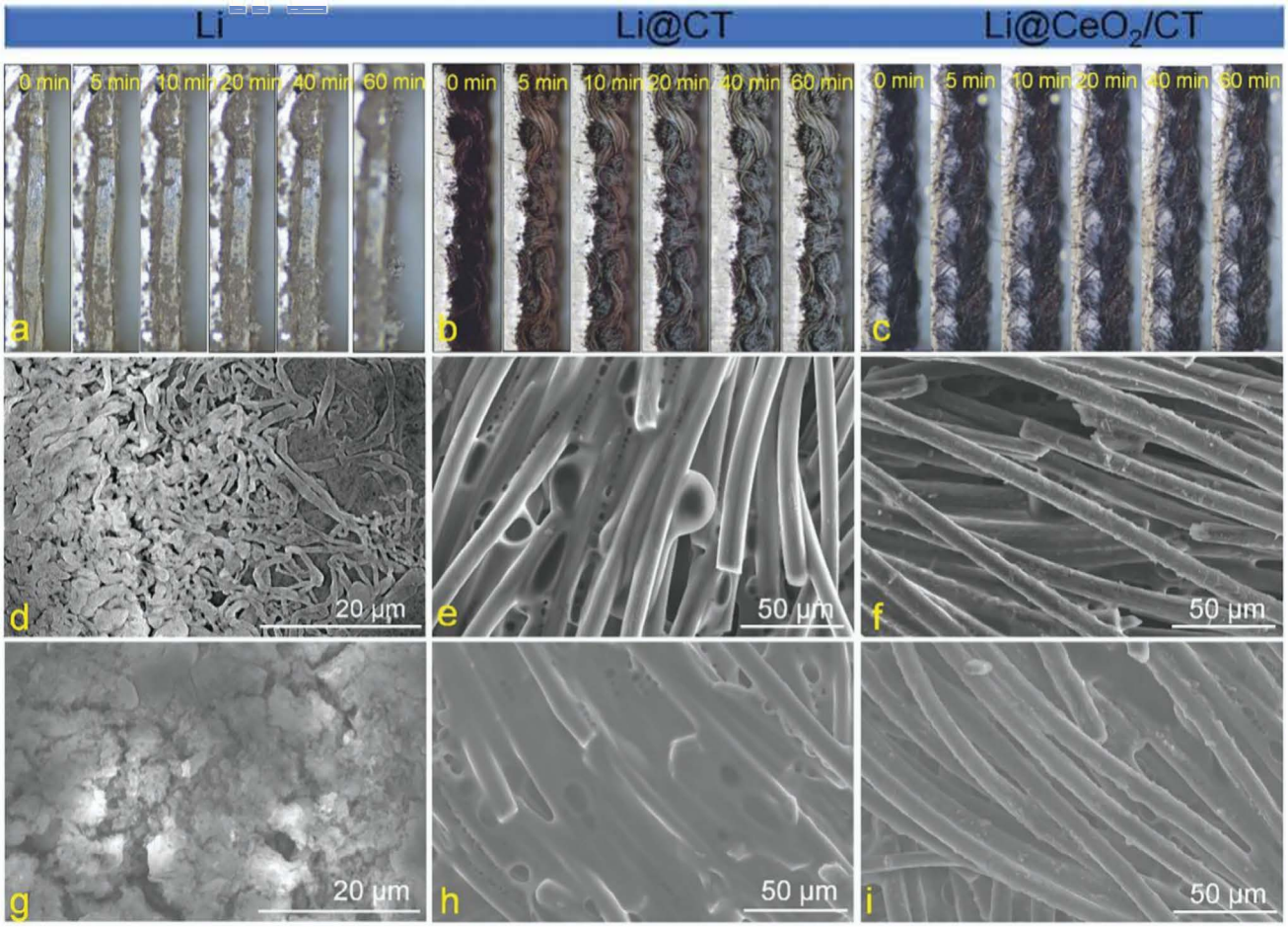

Figure 3. Lithium plating/stripping behavior. Lithium deposition morphology observed under in situ optical microscopy for a) pure Li, b) Li/CT, and c) Li@CeO_2/CT electrodes. SEM morphology of d) pure Li, e) Li@/CT, f) Li@CeO_2/CT electrodes after one cycle at 1 mA cm^{-2} and 1 mAh cm^{-2}, g) pure Li, h) Li@/CT, i) Li@CeO_2/CT electrodes after 20 cycles.

overpotentials emphasizes the effectiveness of CeO_2/CT and CT in promoting a more favorable lithium nucleation process, potentially attributed to their collaborative coupling effect.

To further investigate the underlying mechanism on the composite structure's ability to facilitate uniform Li-ion transport and enhance fast plating/stripping electrochemical performance, X-ray Photoelectron Spectroscopy (XPS) and Transmission Electron Microscopy (TEM) analyses were conducted. The composition of CeO_2/CT after pre-lithiation has been identified, denoted as CeO_x/CT. During the pre-lithiation process, CeO_2 undergoes electrochemical reduction to Ce_2O_3 according to: $2e^- + 2CeO_2 + 2Li^+ \leftrightarrow Ce_2O_3 + Li_2O$.[34] However, due to the specified cutoff voltage of 1.5 V during the charge process, limits the full redox transformation of Ce_2O_3 back to CeO_2. Consequently, both CeO_2 and Ce_2O_3 are expected to coexist in the composite material, forming a heterojunction. This is corroborated by the presence of Ce^{3+} in the XPS spectrum (**Figure 4a**).[35,36] The TEM image reveals that the composite is comprised of small particles with diameters falling within the range of 10–20 nm, which are in close contact with each other (Figure S6, Supporting Information). Furthermore, the electron diffraction patterns of the CeO_x obtained from the TEM analysis provide additional insights. These patterns confirm the coexistence of both CeO_2 and Ce_2O_3 within the composite material (Figure 4b,c), which aligns with the XPS analysis. To verify the affinity and strong interaction between CeO_x and lithium, density functional theory (DFT) calculations were employed to determine the adsorption energy of CeO_x on Li. Differential charge density diagram of carbon and CeO_x absorbed lithium are shown in Figure 4d and Figure S7 (Supporting Information). The adsorption energy of amorphous carbon on lithium were 1.259 eV. In contrast, the adsorption energy of CeO_2 and Ce_2O_3 on different crystal planes demonstrated notably high values (Figure 4e), indicative of a strong affinity for lithium. This observation implies that the carbon fibers coated with CeO_x provide abundant lithiophilic sites, facilitating homogeneous Li ion flux and guiding uniform Li plating/stripping along the CeO_x-coated carbon fibers. To further elucidate the mechanism behind the enhanced Li ion transport, the migration barrier of Li ions in cerium oxides was calculated and compared. As depicted in Figure 4f and Figure S8 (Supporting Information), the Li ion diffusion barriers for Ce_2O_3 and CeO_2 were found to be 1.63 and 1.21 eV, respectively. Intriguingly, the heterojunction formed at the interface of Ce_2O_3 and CeO_2 exhibits the lowest Li ion migration barrier at 1.03 eV. The Li ion migration pathway in

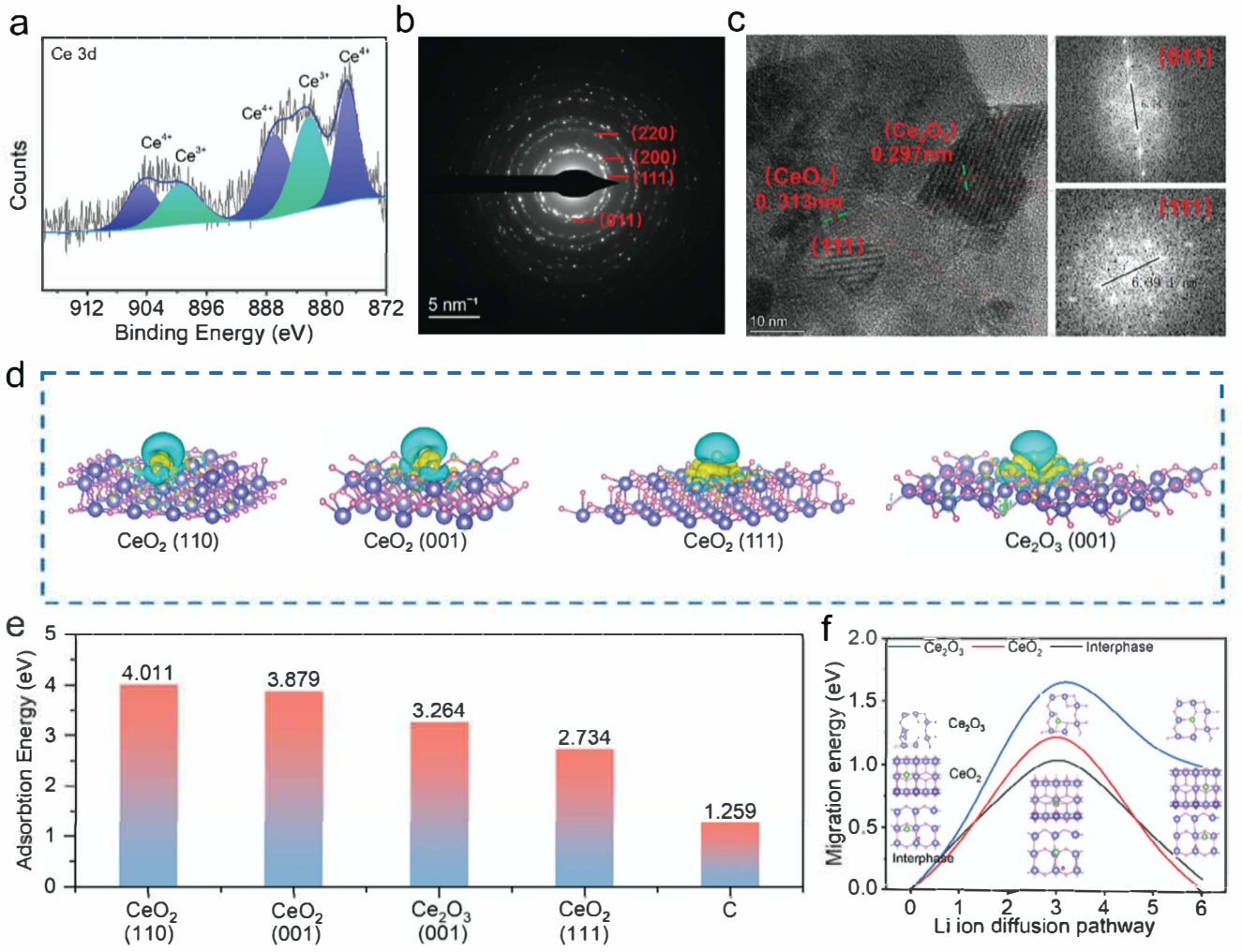

Figure 4. Characterization of CeO_2/CT after pre-lithiation: a) XPS spectrum of Ce 3d. b) TEM characterization of CeO_x, and c) electron diffraction patterns of CeO_x. d) Differential charge density diagram of different crystal planes of CeO_2 and Ce_2O_3 adsorbed lithium and e) corresponding binding energy. f) Li ion diffusion pathway in CeO_2, Ce_2O_3, and the interphase of CeO_2/Ce_2O_3.

different materials is shown in Figure S8 (Supporting Information). This heterojunction, stemming from the coexistence of Ce_2O_3 and CeO_2, effectively enhances the interaction between CeO_x and lithium, facilitating rapid and uniform Li ion diffusion. Simultaneously, the carbon fiber's internal structure serves as an electron current collector, as a result, the unique structure ensures fast electron/ion pathways throughout the entire skeleton. This design enables highly reversible Li plating/stripping during cycling, even under an exceptionally high current density of 100 mA cm^{-2}. The orchestrated interplay between the CeO_x-coated carbon fibers and the heterojunction thus underscores the composite achieving superior electrochemical performance for lithium battery applications.

The lithium plating and stripping behavior on various electrodes are elucidated in **Figure 5**. Regarding to pure Li foil (Figure 5a), the initial lithium deposition is uneven, giving rise to the formation of lithium dendrite "seeds". These dendritic structures serve as initiation points for the continuous expansion of subsequent lithium dendrites, ultimately leading to the accumulation of a substantial amount of "dead lithium." Over prolonged cycling periods, the presence of a large quantity of inactive lithium contributes to rapid capacity fading. Furthermore, the continuous growth of dendrites may penetrate the separator, resulting in a short circuit. Li@CT electrode with high specific surface area and abundant void space can decrease the local current density and accommodates the volume expansion during cycling. However, over extended cycling periods, a challenge emerges. The lithium deposition becomes less uniform along the carbon fiber, leading to accumulation in the void spaces. This uneven distribution and accumulation of lithium may contribute to the formation of "dead lithium", resulting in capacity fading and diminishing overall cell performance (Figure 5b). The uniform coating of CeO_x on the surface of carbon fibers plays a pivotal role in guiding the consistent and stable deposition of lithium metal along the fiber surface. This uniform deposition is facilitated by the heterojunction composed of Ce_2O_3 and CeO_2, which effectively enhances the interaction between CeO_x and lithium, promoting rapid and uniform Li-ion diffusion, and fully use the

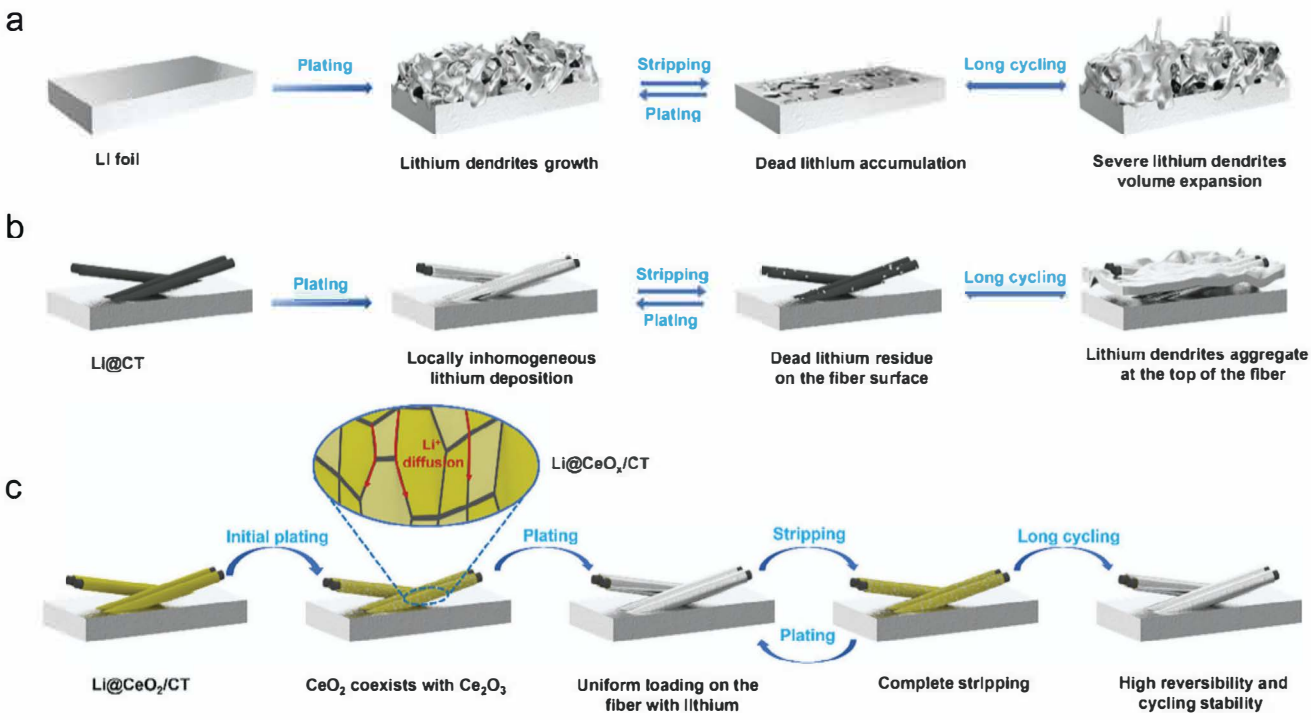

Figure 5. Schematic diagram of lithium plating/stripping behavior in a) pure Li, b) Li@CT, and Li@CeO_2/CT c) electrodes.

large surface area. With the deposition amount increases, lithium metal continues to load uniformly on the substrate. Importantly, even after repeated charge/discharge cycles, lithium metal maintains the ability to achieve uniform deposition and stripping on the fiber surface. This constant uniformity to lithium metal is indicative of the stability and reliability of the Li@CeO_2/CT electrode system during extended cycling process.

To evaluate the compatibility of composite anode in high energy density full cells, the high-nickel content cathode ($LiNi_{0.91}Co_{0.06}Mn_{0.03}O_2$, named as NCM91) was employed as the positive electrode to versus Li, Li/CT, and Li@CeO_2/CT, respectively. Before long-term cycling at 1 C, the cells were cycled at a lower current density of 0.1 C (3 cycles) and 0.5 C (5 cycles), as shown in **Figure** 6a. The Li@CeO_2/CT cell exhibits an initial discharge capacity of 238.3 mAh g^{-1} at 0.1 C and higher initial Coulombic efficiency of 93.97% than that of Li (93.09%) and Li@CT (92.97%). More importantly, the Li@CeO_2/CT cell delivers a more superior cycling stability with a capacity retention of ≈73.4% after 800 cycles (>80% after 600 cycles), comparing to 67.8% for Li@CT and 55.0% for Li, additionally, the average CE reaches 99.94%. The less voltage decay and lower voltage hysteresis in the charge/discharge curve is observed in Li@CeO_x/CT||NCM91 cell (Figure 6b) in comparison to other two type cells (Figure S9, Supporting Information) demonstrating that the reduced cell polarization and more stabilized electrolyte/anode interphase is caused by more robust SEI. To distinguish the fast-charging ability of the full cells effected from different anodes, the rate capability assessment was conducted in the range from 0.1 to 10 C (1 C = 220 mAh g^{-1}). There is no much difference at the low currents (<2 C), however, a clearly capacity drop is observed in the Li||NCM91 once the current increases above 2 C, which is slightly increased for the Li@CT||NCM91 cells. By contrast, the Li@CeO_x/CT||NCM90 cell expresses a much enhanced rate performance at the high rate, the average capacity is 182.6, 169.8, 157.6, 143.0, and 130.1 mAh g^{-1} at 2, 4, 6, 8, and 10 C, respectively, which indicates the cell obtains a capacity of 130.1 mAh g^{-1}, only need charge for 6 mins, which fully demonstrates the excellent fast charging ability contributed by this novel composite anode. The column diagram (Figure 6d) exhibits more intuitively for the advantage of rate capability of Li@CeO_2/CT composite anode. Long-term stability at high current density is generally tough yet crucial performance for the cell configuration, Figure 6e exhibits the cycling performance of different cells at 4 C. The Li@CeO_2/CT||NCM90 cell behaves a much superior cycling stability with capacity retention of 70% after 700 cycles, comparatively, the Li||NCM90 cell only maintains a cycling stability to 200 cycles following a sharply capacity decrease to failure, meanwhile the CE is drastically fluctuant ≈100%, similarly, an obviously performance degradation occurs in the Li@CT||NCM90 cell. This comparison further demonstrates the Li@CeO_2/CT composite anode enabling the high specific energy lithium metal batteries with outstanding fast charging ability contributing to fast ions transport kinetics. To acquire the underlying reason for the superior performance in Li@CeO_2/CT||NCM91 cell, the morphology of cycled electrodes after 800 cycles were investigated by SEM characterization. The pure lithium sheet (Figure 6f) suffered from highly uneven deposition/stripping, resulting in severe damage of the surface structure and the formation of thick lithium dendrites. Meanwhile, the cathode (Figure S10, Supporting Information) occurred severe cracks and even pulverization of the NCM particles, which probably give rise to the severe capacity decay displayed in

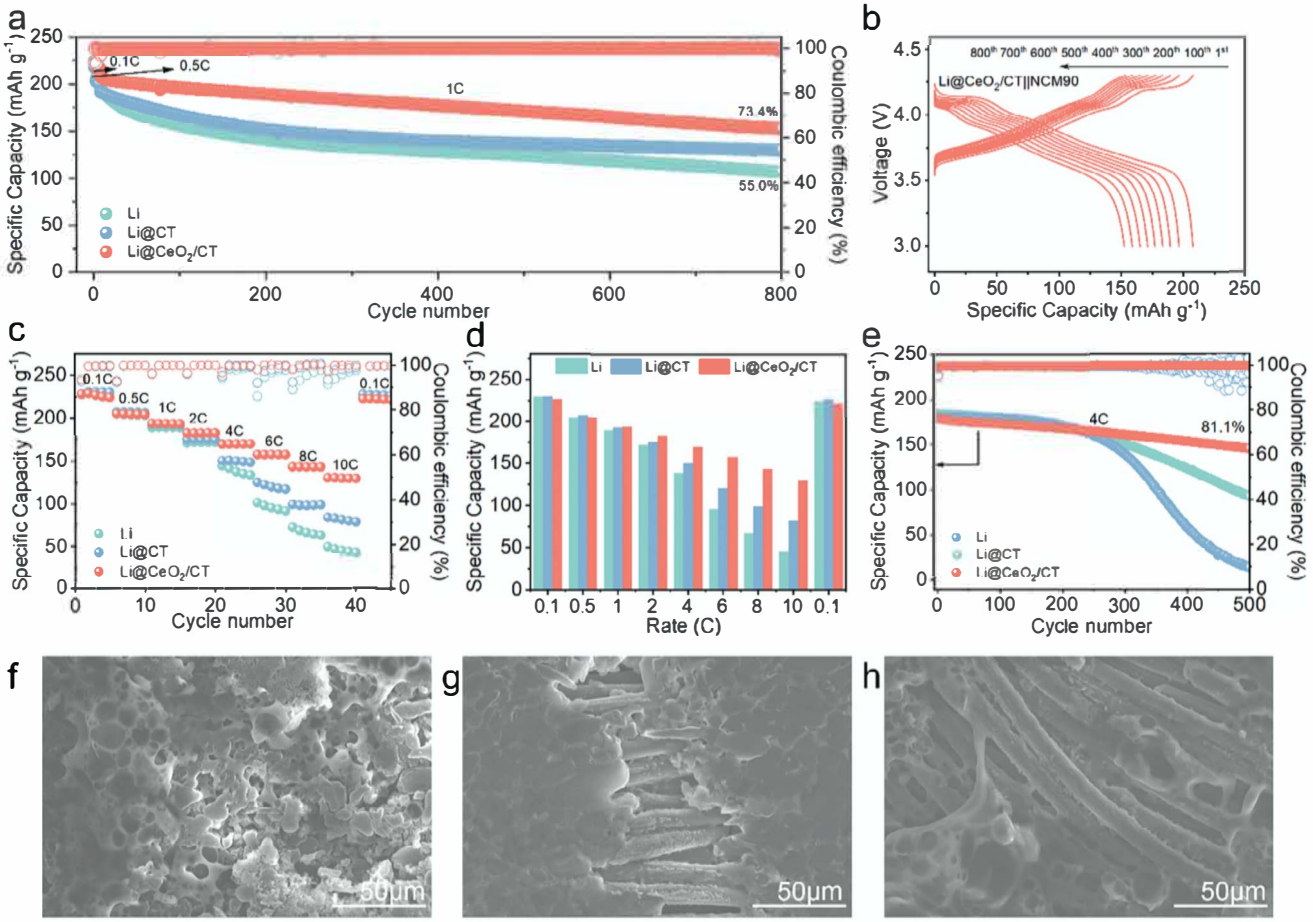

Figure 6. Electrochemical performance of full cells. a) Cycling performance of three different anode based full cells coupled with NCM90 cathode at 1 C rate. b) Selected charge/discharge curves of Li@CeO_2/CT full cell. c,d) Rate performance of different anode based full cell. e) Long cycling performance of three different full cells at 4 C rate. SEM micrography of the electrodes after 800 cycles using f) pure Li, g) Li/CT, and h) Li@CeO_2/CT electrodes.

long-term cycling.[37] In addition, the surface of the Li@CT anode (Figure 6g) shows the thick accumulation of uneven lithium deposition over long cycles, where lithium metal is not deposited along the fibers, instead of forming a thick layer covering the CT fibers. The corresponding cathode particles (Figure S10, Supporting Information) coupled with the Li@CT showed less cracks among the particles. In contrast, the lithium metal almost evenly deposited along the fibers after 800 cycles for the Li@CeO_2/CT anode (Figure 6h), which is ascribed to the uniform loading of lithiophilic CeO_x on the surface of carbon fibers, regulated the homogenous lithium deposited along the fibers. Therefore, the lower interface resistance in turn contributing to more stabilized structure of cathode particles (Figure S10, Supporting Information), allows achieving a more stable cycling performance. We investigated the electrochemical behavior of the electrode within the voltage range of 3.0–4.3 V using cyclic voltammetry. As shown in Figure S11 (Supporting Information), the lithium-ion diffusion coefficients in the full cell were calculated from the CV data at various scan rates. The lithium-ion desorption diffusion coefficient was determined to be 1.81×10^{-7} cm^2 s^{-1}, while the insertion diffusion coefficient was 7.24×10^{-8} cm^2 s^{-1}. The results indicate that the Li@CeO2/CT anode accelerates the kinetics of Li^+ cycling.

To exclude the effect from lithium metal anode, further certify the benefits from CeO_x, the lithium-free cells were assembled with CT and CeO_x/CT anodes and compared in **Figure 7**a. The lithium-free electrode was cycled for five cycles at the current density of 0.5 mA cm^{-2}, in the range of 0.05–1.5 V for the pre-lithiation process, then dissembled the cell and coupled with NCM91. The high cycling stability of CeO_x/CT cells were still obtained with the capacity retention of 87.2% after 200 cycles, exhibits its much superior stability than the CT cells, demonstrating the crucial role of CeO_2 in stabilizing the full cell performance. We also characterized the lithium deposition morphology on the surface of the CeO_x/CT anode after 400 cycles (Figure S12, Supporting Information). There was no significant deposition of lithium metal on the fiber surface, and the Ce and O elements were still uniformly loaded on the fiber surface, indicating that CeO_x maintained its ability to regulate and stabilize charge/discharge activity after prolonged cycling. The comparison of voltage profiles between CT and CeO_x/CT cells clearly exhibit the much less voltage and capacity fading in CT cells, which

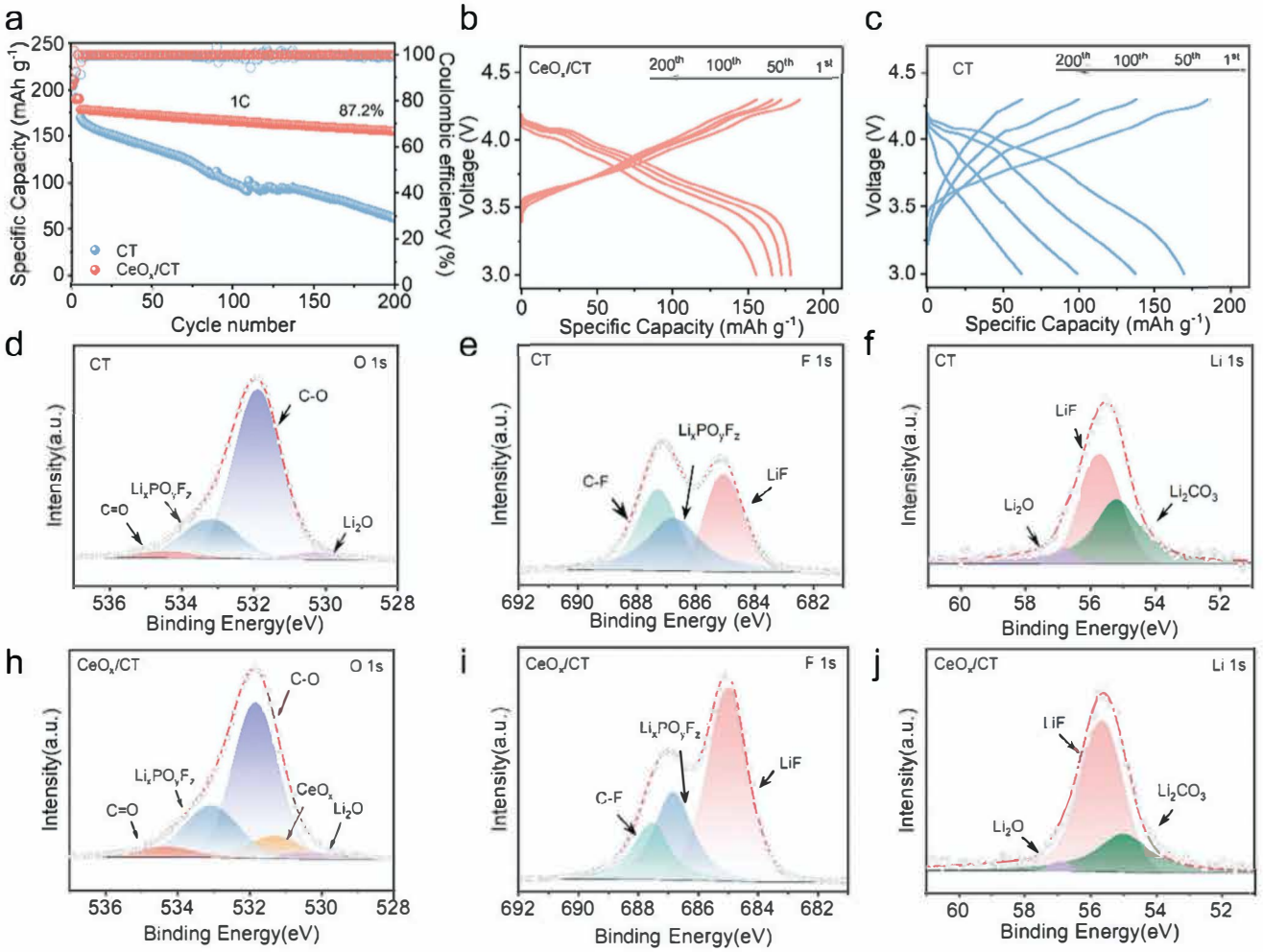

Figure 7. a) Cycling performance and b) the selected voltage curves of lithium-free CeO_x/CT ||NCM91 and c) CT||NCM91 cells. XPS spectra of the surface of the electrode after the lithiation of CeO_x/CT and CT in the d,h) O 1s, e,i) F 1s, and f,j) Li 1s regions, respectively.

also resulted from the suppressed polarization in the CeO_x/CT cells.

2.4. Electrode/Electrolyte Interface Analysis

To figure out the underlying reason for more stabilized electrode/electrolyte interphase in the anode-free CeO_x/CT cell, the X-ray photoelectron spectroscopy (XPS) characterization was carried out to determine the components on the pre-lithiated electrodes. The detailed spectra of CT (top) and CeO_x/CT (bottom) in the O 1s, F 1s, and Li 1s region are compared in Figure 7d–j. In the O 1s spectrum (Figure 7d,h), in addition to common C—O (≈531.9 eV), C═O (≈534.3 eV), $Li_xPO_yF_z$ (≈533.1 eV), and Li_2O (≈530.5 eV), an additional peak was detected at 531.3 eV on the surface of the CeO_x/CT electrode, which can be attributed to the CeO_x adhered on the surface of carbon fiber. Combining with the Ce 3d spectrum (Figure 4a), which indicates that CeO_2 coexist with Ce_2O_3. Therefore, the peak near 531.3 eV in O 1s can be identified as CeO_x. In the F 1s region, an obviously higher LiF (685.0 eV) peak was observed in CeO_x/CT (Figure 7d,i), and the LiF peak in Li 1s spectrum (55.7 eV) also certified the stronger LiF peak in Figure 7e,f. The LiF component contributes to a fluoride-rich SEI layer that has been proven facilitating to lithium transport as well as more robust SEI structure,[38] thus significantly improving the cycle life and suppressing dendrites growth of lithium metal anode.

3. Conclusion

In summary, a high-performance composite anode was designed by uniformly loading lithophilic CeO_2 on CT matrix via a simple rolling method. The heterojunction formed by the in situ generation of CeO_2 and Ce_2O_3 plays a crucial role in reducing the lithium-ion migration barrier. This reduction in energy barrier facilitates the rapid migration of lithium ions within the material. Moreover, both CeO_2 and Ce_2O_3 exhibit high adsorption energies with lithium, signifying strong affinity and interaction with lithium ions. This special designed architecture enables a stable lithium metal deposition/stripping at 100 mA cm^{-2} and 4 mAh cm^{-2}. Moreover, the full cell matched with NCM91 cathode can achieve a capacity retention of 73.4% at 1 C rate after 800 cycles,

and a capacity retention of 87.2% after 200 cycles was also obtained with limited lithium. This simple preparation process and excellent performance design provide a guidance for the future practical application of lithium metal anode.

4. Experimental Section

Synthesis Method: *Preparation of CeO_2/CT*: Cerium nitrate hexahydrate ($CeN_3O_9{\cdot}6H_2O$, 99.95% metals basis), sodium hydroxide (NaOH, AR, 96%) were purchased from Aladdin. Carbon textile (WOS1011 hydrophilic type) was ordered from Taiwan Carbon Energy. Nitric acid (HNO_3 65–68%), and sulfuric acid (H_2SO_4, 96–98%) were purchased from XILONG SCIENTIFIC. The CT was cut into a size of 4 × 4 cm, soaked in a mixed acid (H_2SO_4:HNO_3 = 1:1 vol.%) at 90 °C for 9 h, and then washed alternately with ethanol and deionized water for six times until the acid was removed (all the CT used in this work have been treated with acid washing). After dissolving 1.0416 g $CeN_3O_9{\cdot}6H_2O$ and 0.064 g NaOH in 70 mL deionized water, the CT was immersed in the mixed solution and treated at 220 °C for 24 h. Then the treated CT was placed in a tube furnace and calcinated at 500 °C for 4 h in an Ar atmosphere at a temperature rise rate of 5 °C/min to obtain the treated CeO_2/CT. The mass loading of CeO_2 in CT is ≈1.1 mg cm^{-2}.

Preparation of Li@CeO_2/CT: The entire process was operated in a glove box (O_2 < 0.01 ppm, H_2O < 0.01 ppm) filled with Ar. The fabricated CT was kept at 80 °C for 8 h to completely remove moisture before being transferred to the glove box. A tablet press was used to roll the lithium sheet and CT together to obtain the Li@CeO_2/CT composite anode (Pressure: 6 MPa). For comparison, Li@CT was obtained by rolling the CT without CeO_2 with a lithium sheet using the same process.

Material Characterization: The crystal structures of all samples were measured using XRD (Malvern Panalytical. Empyrean) with Cu Kα radiation. The morphology and element distribution were characterized by field-emission scanning electron microscopy (SEM, Thermo Scientific, Scios$_2$, 20 kV) coupled with an energy dispersive X-ray spectrometer (EDS). The surface chemical analysis was conducted using X-ray photoelectron spectroscopy (XPS, Thermo Scientific K-Alpha). The CeO_x was characterized by transmission electron microscopy (TEM, JEOL JEM-2100Plus, Japan)

Electrochemical Measurements: All electrochemical tests were carried out using CR2032 coin-type batteries assembled in an argon-filled glove box with <0.01 ppm of moisture and oxygen. The electrolyte was 1 M $LiPF_6$ dissolved in ethylene carbonate/diethyl carbonate with fluoroethylene carbonate and vinylene carbonate (EC:DEC = 1:1 Vol.% with 10.0% FEC, 1.0% VC), and commercial PP/PE/PP three-layer composite films (Celgard2325, 25 μm) were used as separators. To fabricate NCM91 cathode for full cell testing, the active material of NCM91 powders were mixed with carbon black (C65) and polyvinylidene fluoride (PVDF) at a weight ratio of 92:4:4 with N-methyl-2-pyrrolidone (NMP) as the solvent. The finally areal mass loading of NCM was ≈3.4 mg cm^{-2}. The cycling performance was carried out on a standard eight-channel Neware battery test system (CT-4008Tn) and LANHE battery test system (CT3002A). EIS measurements were performed on a IVIUM nSTAT multichannel electrochemical workstation in the frequency range from 0.01 Hz to 100 kHz. In situ optical microscopy imaging acquired from optical microscopy to observe in situ microscopic imaging of lithium-ion batteries (LIB-MS, Beijing Scistar technology Co.Ltd) were carried out on a CHI 660E.

Theoretical Calculation: The Vienna ab initio simulation package (VASP) was employed for our calculations,[39,40] which utilized projector augmented wave (PAW) potentials to describe the interactions between valence electrons and ions.[41] The calculation of the exchange-correlation energy of electrons was performed using the Perdew–Burke–Ernzerhof (PBE) parameterization within the generalized-gradient approximation (GGA). A kinetic energy cutoff of 450 eV was employed for the plane-wave basis.[42] Amorphous carbon, CeO_2, and Ce_2O_3 slabs were modeled using a 2 × 2 × 1 Gamma-centered grid in the Brillouin zone[43] In this work, amorphous carbon was represented by single-layer graphites. The heterojunction composed of CeO_2 and Ce_2O_3 is formed by splicing their respective (1 1 1) faces, and a vacuum space of 15 Å was utilized above the surfaces to prevent interactions from the periodic system. The climbing image nudged elastic band (CI-NEB) (Henkelman et al., 2000) approach was employed to calculate the transition state of Li diffusion. All internal atomic positions were fully relaxed in a constant supercell volume and shape until the energy and force convergence threshold of 10–5 eV and 0.03 eV $Å^{-1}$, respectively.

Acknowledgements

Project funded by the National Natural Science Foundation of China (52161039, 52062035, and 12305327), the Jiangxi Provincial Natural Science Foundation (20224BAB204011, 20224BAB214011, 20232BAB211028, 20212BAB214053, 20223BBE51028, and 20223BBE51022). The Talent Project of Double Thousands Plan in Jiangxi Province (jxsq2020101056). Prof. Ortiz acknowledges the Scientific Research Funds of Huaqiao University (605-50Y23030).

Conflict of Interest

The authors declare no conflict of interest.

Author Contributions

S.F. conceptualized the experiment, data analysis, manuscript writing and provided funding for the work. H.S.W. performed materials preparation and characterization, electrochemical measurements, manuscript writing. S.Q.Z. performed the DFT calculation, data analysis. M.M.Y. performed the characterization and electrochemical measurements. X.L. data analysis and revised the manuscript. Y.L. revised the manuscript. F.L.W. per-formed the electrochemical measurements, co-writing and revised the manuscript. W.H.Z. revised the manuscript, N.G.Z. performed the DFT calculation, provided funding and revised the manuscript. G. F.O. concep-tualized and coordinated the activities, and revised the manuscript.

Data Availability Statement

The data that support the findings of this study are available from the corresponding author upon reasonable request.

Keywords

CeO_2, composite lithium anode, Fast charging, heterojunction, lithium metal batteries

[1] C. Liu, F. Li, L. P. Ma, H. M. Cheng, *Adv Mater* **2010**, *22*, E28.

[2] Q. H. Huang, A. Zeb, Z. H. Xu, S. Sahar, J. E. Zhou, X. M. Lin, Z. Y. Wu, R. C. K. Reddy, X. Xiao, L. Hu, *Coord. Chem. Rev.* **2023**, *494*, 215335.

[3] J. E. Zhou, J. H. Chen, Y. H. Peng, Y. Q. Zheng, A. Zeb, X. M. Lin, *Coord. Chem. Rev.* **2022**, *472*, 214781.

[4] M. S. Whittingham, *Chem. Rev.* **2014**, *114*, 11414.
[5] C. P. Grey, J. M. Tarascon, *Nat. Mater.* **2017**, *16*, 45.
[6] P. G. Bruce, S. A. Freunberger, L. J. Hardwick, J. M. Tarascon, *Nat. Mater.* **2012**, *11*, 19.
[7] W. Xu, J. L. Wang, F. Ding, X. L. Chen, E. Nasybutin, Y. H. Zhang, J. G. Zhang, *Energy Environ. Sci.* **2014**, *7*, 513.
[8] J. E. Zhou, Z. H. Xu, Y. L. Li, X. M. Lin, Y. B. Wu, A. Zeb, S. G. Zhang, *Coord. Chem. Rev.* **2023**, *494*, 215348.
[9] R. C. K. Reddy, X. M. Lin, A. Zeb, C. Y. Su, *Electrochem. Energy Rev.* **2022**, *5*, 312.
[10] Q. Wang, B. Liu, Y. Shen, J. Wu, Z. Zhao, C. Zhong, W. Hu, *Adv. Sci.* **2021**, *8*, 2101111.
[11] F. Wu, Z. Chen, S. Fang, W. Zuo, G.-T. Kim, S. Passerini, *Energy Storage Mater.* **2023**, *63*, 103062.
[12] M. A. Hope, B. L. D. Rinkel, A. B. Gunnarsdóttir, K. Märker, S. Menkin, S. Paul, I. V. Sergeyev, C. P. Grey, *Nat. Commun.* **2020**, *11*, 2224.
[13] D. T. Boyle, W. Huang, H. S. Wang, Y. Z. Li, H. Chen, Z. Yu, W. B. Zhang, Z. N. Bao, Y. Cui, *Nat. Energy* **2021**, *6*, 487.
[14] A. Kolesnikov, M. Kolek, J. F. Dohmann, F. Horsthemke, M. Boerner, P. Bieker, M. Winter, M. C. Stan, *Adv. Energy Mater.* **2020**, *10*, 2000017.
[15] D. C. Lin, Y. Y. Liu, Y. Cui, *Nat. Nanotechnol.* **2017**, *12*, 194.
[16] R. Zhang, X. Shen, X. B. Cheng, Q. Zhang, *Energy Storage Mater.* **2019**, *23*, 556.
[17] M. Siniscalchi, J. L. Liu, J. S. Gibson, S. J. Turrell, J. Aspinall, R. S. Weatherup, M. Pasta, S. C. Speller, C. R. M. Grovenor, *ACS Energy Lett.* **2022**, *7*, 3593.
[18] R. Zhang, X. Shen, H. T. Ju, J. D. Zhang, Y. T. Zhang, J. Q. Huang, *J. Energy Chem.* **2022**, *73*, 285.
[19] Y. H. Liu, J. M. Sun, X. Q. Hu, Y. F. Li, H. F. Du, K. Wang, Z. Z. Du, X. Gong, W. Ai, W. Huang, *Nano Energy* **2022**, *94*, 106883.
[20] X. X. Ma, X. Chen, Y. K. Bai, X. Shen, R. Zhang, Q. Zhang, *Small* **2021**, *17*, 2007142.
[21] Y. X. Zhan, P. Shi, R. Zhang, X. Q. Zhang, X. Shen, C. B. Jin, B. Q. Li, J. Q. Huang, *Adv. Energy Mater.* **2021**, *11*, 2101654.
[22] Y. Zhao, T. H. Zhou, T. Ashirov, M. El Kazzi, C. Cancellieri, L. P. H. Jeurgens, J. W. Choi, A. Coskun, *Nat. Commun.* **2022**, *13*, 2575.
[23] J. Chen, X. L. Fan, Q. Li, H. B. Yang, M. R. Khoshi, Y. B. Xu, S. Hwang, L. Chen, X. Ji, C. Y. Yang, H. X. He, C. M. Wang, E. Garfunkel, D. Su, O. Borodin, C. S. Wang, *Nat. Energy* **2020**, *5*, 386.
[24] R. Pathak, K. Chen, A. Gurung, K. M. Reza, B. Bahrami, J. Pokharel, A. Baniya, W. He, F. Wu, Y. Zhou, K. Xu, Q. Qiao, *Nat. Commun.* **2020**, *11*, 93.
[25] W. Guo, W. Y. Zhang, Y. B. Si, D. H. Wang, Y. Z. Fu, A. Manthiram, *Nat. Commun.* **2021**, *12*, 3031.
[26] S. Fang, F. Wu, S. Zhao, M. Zarrabeitia, G. T. Kim, J. K. Kim, N. Zhou, S. Passerini, *Adv. Energy Mater.* **2023**, *13*, 2302577.
[27] H. Chen, Y. F. Yang, D. T. Boyle, Y. K. Jeong, R. Xu, L. S. de Vasconcelos, Z. J. Huang, H. S. Wang, H. X. Wang, W. X. Huang, H. Q. Li, J. Y. Wang, H. K. Gu, R. Matsumoto, K. Motohashi, Y. Nakayama, K. J. Zhao, Y. Cui, *Nat. Energy* **2021**, *6*, 790.
[28] D. C. Lin, Y. Y. Liu, Z. Liang, H. W. Lee, J. Sun, H. T. Wang, K. Yan, J. Xie, Y. Cui, *Nat. Nanotechnol.* **2016**, *11*, 626.
[29] S. Zhang, S. Y. Xiao, D. P. Li, J. L. Liao, F. J. Ji, H. B. Liu, L. J. Ci, *Energy Storage Mater.* **2022**, *48*, 172.
[30] Y. Zhou, Y. Han, H. T. Zhang, D. Sui, Z. H. Sun, P. S. Xiao, X. T. Wang, Y. F. Ma, Y. S. Chen, *Energy Storage Mater.* **2018**, *14*, 222.
[31] S. F. Liu, X. H. Xia, Z. J. Yao, J. B. Wu, L. Y. Zhang, S. J. Deng, C. G. Zhou, S. H. Shen, X. L. Wang, J. P. Tu, *Small Methods* **2018**, *2*, 2800035.
[32] P. Du, C. B. Yuan, X. Y. Cui, K. F. Zhang, Y. Yu, X. D. Ren, X. W. Zhan, S. Gao, *J. Mater. Chem. A* **2022**, *10*, 8424.
[33] S. Fang, L. Shen, A. Hoefling, Y. Wang, G. Kim, P. A. van Aken, X. Zhang, S. Passerini, *Nano Energy* **2021**, *89*, 106421.
[34] Q. M. Su, L. Chang, J. Zhang, G. H. Du, B. S. Xu, *J. Phys. Chem. C* **2013**, *117*, 4292.
[35] D. Nikolova, E. Stoyanova, D. Stoychev, P. Stefanov, T. Marinova, *Surf. Coat. Technol.* **2006**, *201*, 1559.
[36] X. Liu, X. Zheng, Y. Dai, W. Wu, Y. Huang, H. Fu, Y. Huang, W. Luo, *Adv. Funct. Mater.* **2021**, *31*, 2103522.
[37] F. Wu, A. Mullaliu, T. Diemant, D. Stepien, T. N. Parac-Vogt, J. K. Kim, D. Bresser, G. T. Kim, S. Passerini, *InfoMat* **2023**, *5*, 12462.
[38] F. Wu, S. Fang, M. Kuenzel, A. Mullaliu, J.-K. Kim, X. Gao, T. Diemant, G.-T. Kim, S. Passerini, *Joule* **2021**, *5*, 2177.
[39] G. Kresse, J. Furthmuller, *Phys. Rev. B* **1996**, *54*, 11169.
[40] G. Kresse, D. Joubert, *Phys. Rev. B* **1999**, *59*, 1758.
[41] P. E. Blochl, *Phys. Rev. B* **1994**, *50*, 17953.
[42] J. P. Perdew, K. Burke, M. Ernzerhof, *Phys. Rev. Lett.* **1997**, *78*, 1396.
[43] H. J. Monkhorst, J. D. Pack, *Phys. Rev. B* **1976**, *13*, 5188.